actuators

MDPI

Article

A Fault Diagnosis Approach for Electromechanical Actuators with Simulating Model under Small Experimental Data Sample Condition

Zhaoqin Peng [1], Zhengyi Sun [1], Juan Chen [2,*], Zilong Ping [2], Kunyu Dong [1], Jia Li [3], Yongling Fu [2] and Enrico Zio [4,5]

[1] School of Automation Science and Electrical Engineering, Beihang University, Beijing 100191, China; pengzhaoqin@buaa.edu.cn (Z.P.); szy145024@buaa.edu.cn (Z.S.); dongkunyu@buaa.edu.cn (K.D.)
[2] School of Mechanical Engineering and Automation, Beihang University, Beijing 100191, China; zilongping@buaa.edu.cn (Z.P.); fuyongling@buaa.edu.cn (Y.F.)
[3] Energy Department, Politecnico di Milano, Piazza Leonardo da Vinci, 3220133 Milano, Italy; jia.li@polimi.it
[4] Energy Department, MINES Paris Tech, 60 Bd St Michel, 75006 Paris, France; enrico.zio@polimi.it
[5] Energy Department, PSL Research University, 60 Rue Mazarine, 75006 Paris, France
* Correspondence: chen.juan@buaa.edu.cn

Abstract: Electromechanical actuators (EMAs) have shown a high efficiency in flight surface control with the development of more electric aircraft. In order to identify the abnormalities and potential failures of EMA, a methodology for fault diagnosis is developed. A simulating model of EMA is first built to perform different working states. Based on the modeling of EMA, the corresponding faults are then simulated to re-generate the fault data. Afterwards, a gated recurrent unit (GRU) and co-attention-based fault diagnosis approach is proposed to classify the working states of EMA. Experiments are conducted and a satisfying classification accuracy on simulated data is obtained. Furthermore, fault diagnosis on an actual working system is performed. The experimental results demonstrate that the proposed method has a high efficiency.

Keywords: electromechanical actuators; fault diagnosis; small sample; gate recurrent unit; co-attention mechanism

Citation: Peng, Z.; Sun, Z.; Chen, J.; Ping, Z.; Dong, K.; Li, J.; Fu, Y.; Zio, E. A Fault Diagnosis Approach for Electromechanical Actuators with Simulating Model under Small Experimental Data Sample Condition. *Actuators* **2022**, *11*, 66. https://doi.org/10.3390/act11030066

Academic Editor: Ignazio Dimino

Received: 19 January 2022
Accepted: 16 February 2022
Published: 22 February 2022

1. Introduction

Recently, more electric aircraft (MEA) initiatives have focused on increasing the penetration of the electrical systems into the aircrafts, in order to decrease the weight and increase the overall efficiency [1,2]. Once restricted to airborne hydraulic distribution systems, the move towards MEA has considerably progressed with advances in electrically powered actuators. Electromechanical actuators (EMAs) present a solution which exploits a mechanical drivetrain to reach the control surface [3]. Compared with the alternatives (e.g., classical hydraulic systems and electro-hydrostatic actuators), the EMAs simply control the motor and leverage on a planetary roller screw pair to translate the rotary motion into linear motion, which has brought paradigm shifts to power the MEA transmission. As one of the commercial aircrafts, the Boeing 787 applies EMAs to landing gear braking, a spoiler, as well as a trimmable horizontal stabilizer [4,5].

In spite of the reduced complexity and easy maintenance, EMAs are currently used in fewer safety-critical control surfaces or tasks with redundant alternatives [6]. This is due to the fact that the failure risks and accumulated reliability experience are absent [7]. That is, the latent failures of EMAs relegate them to still be implemented on secondary flight controls. Consequently, the fault diagnosis of EMA is mostly studied, which paves the way for deeply understanding the fault occurrence and its principle [8,9].

Theoretically, fault diagnosis aims at detecting and identifying any type of potential abnormalities and faults [10,11]. Numerous artificial intelligence techniques and statistical

learning methods have been widely used in fault diagnosis, such as k-nearest neighbor (k-NN) algorithms [12], Bayesian classifier [13], support vector machine (SVM) [14], and deep learning approaches [15]. In recent years, deep-learning algorithms have underpinned the state-of-the-art implementations for fault diagnosis tasks [16,17]. More precisely, the deep-learning-based methods use a large number of samples for model training, based on which they predict the underlying failures [18,19]. Consequently, a set of complete data that represent both normal and faulty cases is required [20]. However, fault data collection in EMA remains challenging, especially in expensive and precise components, which cannot be threatened to recreate fault occurrences. Furthermore, failure tests on EMAs in actual working conditions are highly-priced and time-consuming, which also poses a major limitation of data-based fault describing and distinguishing [21]. For these reasons, the system virtual simulating is highlighted [22]. As mentioned in [23], 'virtual simulation is defined as the creation of interactive environments that replicate a real-world scenario'. Using the virtual simulator, the dynamic model of EMA can be devised and the faults can be injected [24,25]. Therefore, the signals that characterize the EMA working states are measured by virtual sensing elements in simulated tests, which provides opportunities to collect samples for fault diagnosis model training.

This paper develops a virtual simulator in line with the functionalities of EMA in practical working conditions, while focusing on the components' failure principle to generate and inject faults into the simulated model. For fault diagnosis, a deep-learning-based network is proposed, while the fault data are collected for model training. Fault signals from both simulation tests and in-service EMA are measured and sent to the proposed model, to verify the efficiency of the proposed fault diagnosis method.

The remainder of this paper is organized as follows. The background knowledge of EMA is presented in Section 2. Section 3 details the virtual simulator of EMA. The deep-learning based fault diagnosis model is presented in Section 4. The experimental results are provided in Section 5. Finally, the conclusions are drawn in Section 6.

2. Prerequisite

2.1. Architecture of EMA

The schematic diagram of EMA is presented in Figure 1. In general, an EMA is made up of a mechanical actuating assembly and an electronic controller. More precisely, the mechanical actuating assembly consists of a servo motor and mechanical transmission components (i.e., a planetary roller screw pair), to convert the electric drive into mechanical power [26]. The controller is used to determine the current by voltage pulse width modulation (PWM) to the motor, according to the position demand. The motor rotates forward and in reverse in line with the output control commands from the controller [27]. The planetary roller screw pair then converts the rotational motion into linear movement of the EMA rod end [28]. In response, signals of position, velocity, and current are detected and sent to the controller as feedback.

2.2. Faults in EMA

The malfunction information of EMAs mainly comes from the following sources: Failure Modes, Effects, Criticality Analysis (FMECA) information provided by Moog Corporation [21], reports from US military programs [29–31], and general survey of publications involved with EMA diagnostics [16–20].

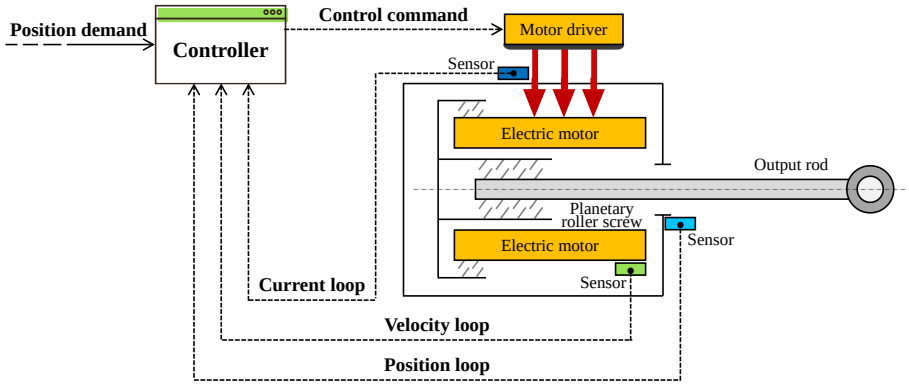

Figure 1. EMA schematic diagram.

In general, four categories of faults exist in EMA: motor, mechanical system, sensor and electronics. To the best of our knowledge, motor malfunction is the most important among all these faults. With respect to the motor components, the failure probability of bearings is 41% following with the stator accounting for 37%. More precisely, almost 80% stator failures result from winding insulation faults. A small inter-phase short circuit or short to ground can also lead to the collapse of the flight control system, which is more severe than the damage of bearings. Therefore, a sensor that detects the motor current is also used to monitor the working state. Several current studies deal with the electrical failures of the motor in EMA.

2.3. Fault Diagnosis of EMA

Fault diagnosis of EMAs has received a certain amount of interest in recent years. Despite the lack of reliable fault statistics, state-of-the-art methods work on detecting the faults of components before the system evolves into catastrophic consequences. Specifically, Yu et al. proposed the concept of extended analytical redundancy relations, based on which a fault diagnosis approach is developed for nonparametric fault identification of electromechanical systems [20]. Moreover, Daniele et al. applied the fuzzy inference system to detect failures on the electric motor of EMAs [16]. Aiming to predict multiple failure modes, Zhang et al. estimated the EMA working data on both the simulation model and experiment platform of EMA [32]. Notably, studies on deep-learning-based EMA fault recognition models are ongoing. Siahpour et al. devised a CNN-based model across distinguishing sensing data [18]. Likewise, Zhang et al. proposed a method by integrating a gated recurrent unit, attention mechanism, and similarity measure. In addition, a model based on a sparse feature and long short-term memory network has been developed [19]. With the faults injected, experimental results validated the working performance of the deep learning method.

3. EMA Simulator

3.1. Simulation Model Development

For the purpose of fault diagnosis, an EMA simulator is first developed to inject fault data into it. The virtual model of EMA is constructed in line with the actual EMA to simulate its working states, as illustrated in Figure 2. As previously mentioned, the mechanical assembly of the proposed EMA model contains a reduction gear, a bearing, and a planetary roller screw, while the electrical components are a triple-loop controller, a permanent magnet synchronous motor (PMSM), together with the motor drive. The control command is transformed into the motor torque and rotating speed, and therefore drives the movement of the screw through the mechanical assembly. The moving relationship of the mechanical drivetrain is performed using mathematical equations.

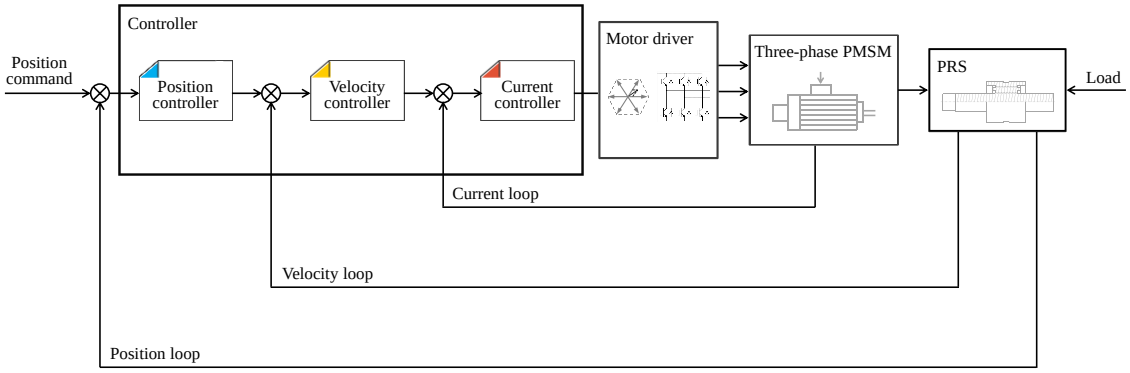

Figure 2. EMA Simulator.

The mechanical assembly: considering the working principle of EMA, the planetary roller screw is the key component which aims to match the torque and speed between the motor and the external load by transitional mechanism [26]. Mathematically, the motion o

$$v_s = \frac{p}{2\pi}\omega_m \tag{1}$$

$$F_s = \frac{2\pi}{p}T_m \tag{2}$$

where v_s and F_s, respectively, represent the axial speed and output force of the screw, ω_m and T_m, respectively, denote the torque and rotating speed of the motor, and p is the lead of planetary roller screw.

The energy loss within the transmitting pairs should also be considered, including the inertia effect, friction loss. The inertia of the planetary roller screw is negligible in the system and is equivalently converted to that of the motor rotor. The friction loss can be simplified proportionally to the rotating speed, known as viscous friction. Consequently, the motion of the mechanical drivetrain is given by:

$$F_s = \frac{2\pi}{p}(T_m - J\frac{d\omega_m}{dt} - B_m\omega_m) \tag{3}$$

where J and B_m, respectively, represent the inertia moment and viscous friction coefficient equivalent to the motor rotor.

The model of mechanical assembly, containing a planetary roller screw, sensing elements, and the external load, is developed in AMESim; see Figure 3. All the components are obtained from the AMESim standard library, while the load is given by directly inputting dynamic force.

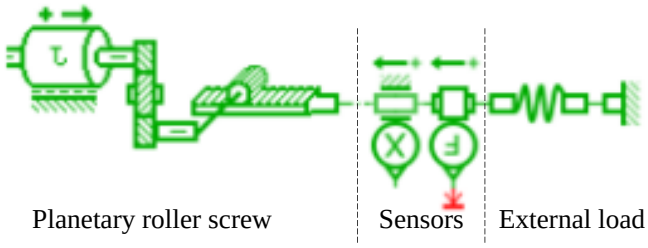

Figure 3. Mechanical assembly model.

The electrical module: the electrical module is mainly used to transform the control command into the mechanical assembly inputs for actuating. The triple-loop controller contains three control units: a position controller, a velocity controller, and a current controller (see Figure 2 for details). The current controller exploits the spatial vector control

to meet the requirement of high-frequency switching of the motor driver. Circular rotating magnetic field generated by a space vector are dedicatedly designed to improve the tracking accuracy of the current loop. The speed and position loops use the Proportional Integral (PI) control, which ensures the settling time and the steady-state accuracy.

Furthermore, a three-phase inverter and six Insulated Gate Bipolar Transistor (IGBTs) are used as the motor driver. The three-phase inverter receives the PWM signals from the spatial vector controller, regulates the on-off switching of all the IGBTs, and thus delivers a three-phase sinusoidal voltage to the motor stator.

In line with the three-phase voltage on the stator, the rotating speed and the electromagnetic torque of rotor are generated. The transformation between the two-phase rotating reference frame (dq) and the three-phase stationary coordinate system (abc) is performed using the constant-power Clarke and Park transformation and inverse transformation:

$$u_d = R_s i_d + L_d \frac{di_d}{dt} - \omega_m L_q i_q \tag{4}$$

$$u_q = R_s i_q + L_q \frac{di_q}{dt} + \omega_m L_d i_d + \sqrt{\frac{3}{2}} \omega_m \varphi_f \tag{5}$$

$$T_m = -n(\sqrt{\frac{3}{2}} i_q \varphi_f + (L_d - L_q) i_q i_d) \tag{6}$$

where u, L, and i, respectively, represent the voltage, inductance, and current of dq coordinate, R_s denotes the equivalent resistance of each stator winding, φ_f is the permanent magnet flux linkage, and n is the number of the motor pole-pairs.

The overall EMA model, containing the mechanical assembly and the electrical module, is built on the platform of AMESim (see Figure 4 for details). The motor and its driver are devised using standard components, while the hysteresis controller and PI controllers are developed based on mathematical expressions. More precisely, all the key parameters of EMA, such as the equivalent moment of inertia to the rotor and screw viscous damping coefficient, as well as the control parameters of the PI controller, are identified using a differential evolution algorithm [33].

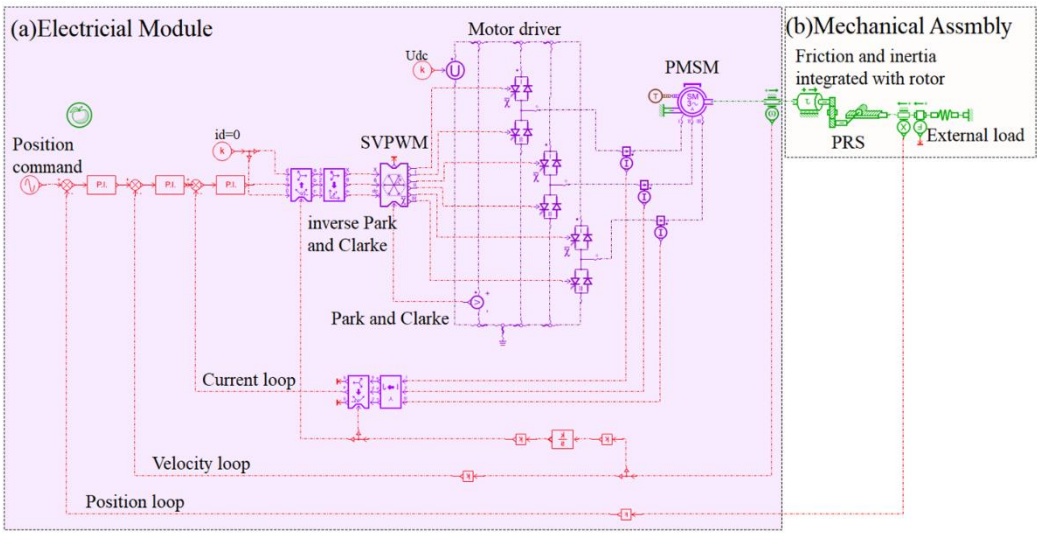

Figure 4. The simulation model of EMA.

3.2. Simulation Model Verification

The efficiency of the proposed EMA model in failure simulation is assessed. The simulation parameters are obtained based on the differential evolution algorithm [33,34]. Each parameter presented in Table 1 obtains an optimal value after the differential evolution.

Table 1. Specifications for EMA model simulation.

Parameter	Notation	Value
Three-phase inverter voltage (V)	U	310
Screw lead (m)	p	0.00254
Equivalent moment of inertia to rotor (kg·m^2)	J	0.0026
Equivalent viscous friction coefficient to rotor (Nm/(rad/s))	B_m	0.5
Equivalent resistance value of each stator winding (ohm)	R_s	2.26
Permanent magnet flux (Wb)	φ_f	0.2375
Number of pole pairs	n	4

A step signal: $y = \begin{cases} 10,\ 0.8s < t < 2.4s \\ 0,\ 0s < t < 0.8s, 2.4s < t < 4s, 5.6s < t < 6s \\ -10,\ 4s < t < 5.6s \end{cases}$ and a sinusoidal signal $y = 2sin(2\pi \times 2t)$ are sent to the model as the reference to evaluate the tracking performance. The simulated tracking outcomes are presented in Figure 5.

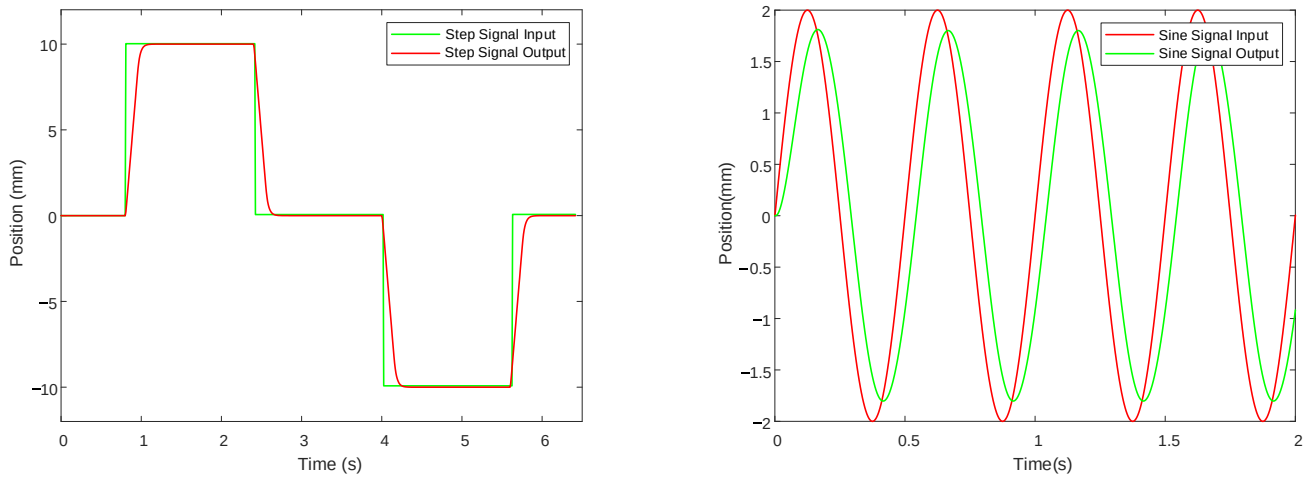

(**a**) (**b**)

Figure 5. Simulation response to different inputs. (**a**) Response to step input; (**b**) Response to sinusoidal input.

In terms of step signals, system overshoot, steady-state error, and settling time are typically employed to characterize the tracking accuracy. During the input signal drop from 0 to −10 mm, the steady-state error is less than 0.2% with the settling time of 0.20 s. When the input jumps to 10 mm, the steady-state error varies within 0.3%, and the settling time is 0.21 s. No overshoot is generated during tracking. For the 2 Hz sine input signal, amplitude attenuation and phase lag of the proposed model are computed, which are 0.18 mm and 28.1° within the stabilization. The simulation results demonstrate that the proposed model has a satisfying performance in both tracking accuracy and settling time. Consequently, the proposed EMA simulator can be applied to the fault injecting process for fault data generation.

4. EMA Fault Diagnosis Method

At this stage, a sine signal is considered as the control command of EMA, whose amplitude is 2 mm and the frequency ranges from 0.3 Hz to 6 Hz with an interval of 0.3 Hz. The external load is of 0 N and 500 N.

Forty sets of different working conditions are performed. The three-phase current of the motor is measured to characterize the working state of EMA. Notably, all these

40 sets of data refer to general working conditions while singular condition is currently not considered.

4.1. Fault Injection

As previously mentioned, the open circuiting of the motor stator is a serious fault to the control system and motor, which accounts for a high proportion of all the EMA faults. Therefore, the motor open circuit malfunction is simulated, containing an open circuit of stator windings and IGBT in motor driver. In general, the unstable power supply, ground faults, and mechanical vibrating shock can result in the disconnection. An open circuit in phase A indicates the current of this phase approaches 0, as shown in Figure 6. Consequently, the current summation of the other two phases is also equal to 0. Using this property, the open circuit fault is injected into the EMA simulator. Specifically, an electric switch is inserted to A phase to control the output current, as presented in Figure 7. With the fault injected, the current of phase A is 0 while those of the other phases tremendously increases. Figure 8 exhibits the three-phases current of A-phase open circuit while the normal state data is also given for comparison.

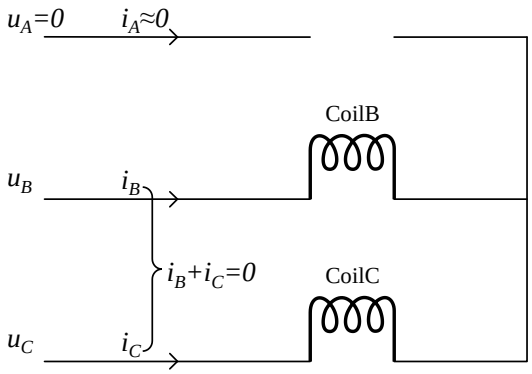

Figure 6. A-phase open circuit.

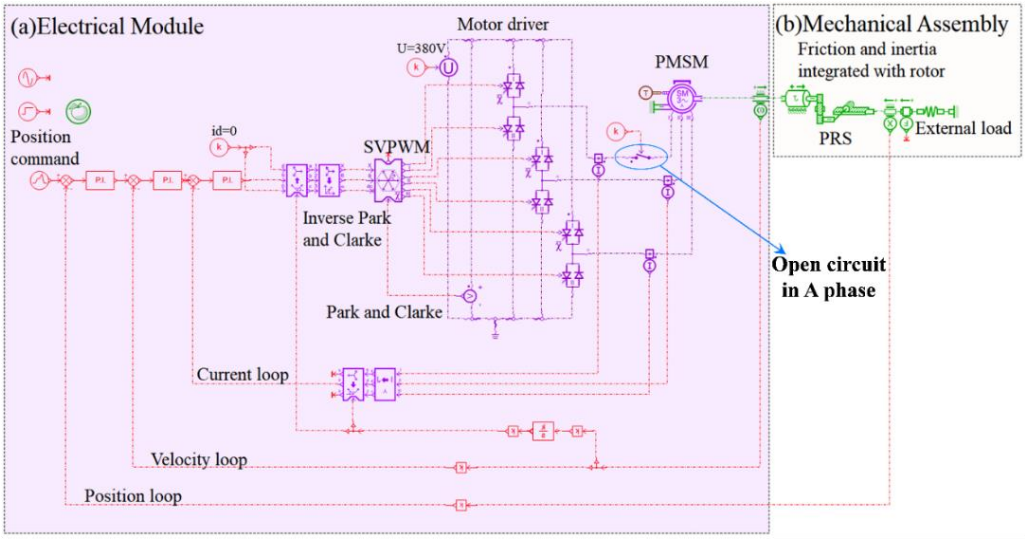

Figure 7. Open circuit fault injection. (**a**) Electrical Module. (**b**) Mechanical Assembly.

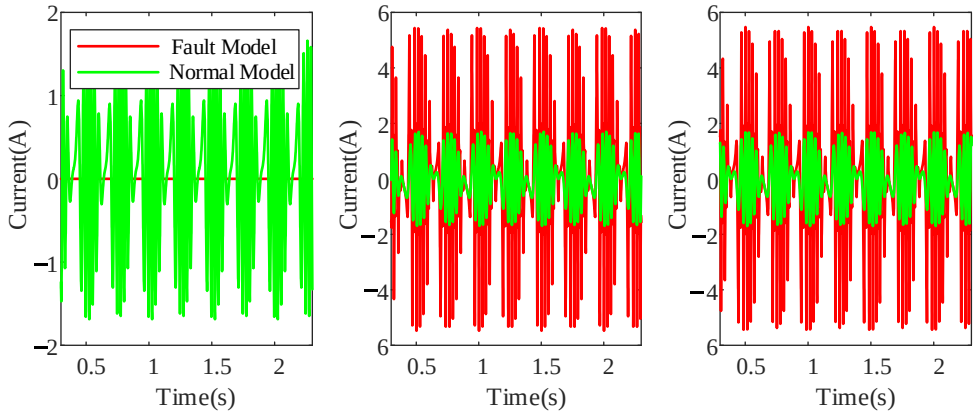

Figure 8. Fault data of A-phase open circuit. (**a**) A-phase current; (**b**) B-phase current. (**c**) C-phase current.

A-phase open circuit represents $i_A \approx 0$ and $i_B + i_C = 0$.

On the other hand, the IGBTs of the inverter work in a high-voltage condition, which generate a large amount of heat during the high-frequency switching. Therefore, the IGBTs always suffer from the alternation of cold and heat, and are therefore subjected to continuous shear stress. Due to the fact that two IGBTs exist for each phase, each IGBT has the risk of disconnection during the work process. Hence, the faults are defined as the open circuit of upper-bridge IGBT (Figure 9a), lower-bridge IGBT (Figure 9b), and both IGBTs (Figure 9c) of each phase. The open circuit of IGBT will result in increasing the phase voltage and phase current, and further lead to the motor instability.

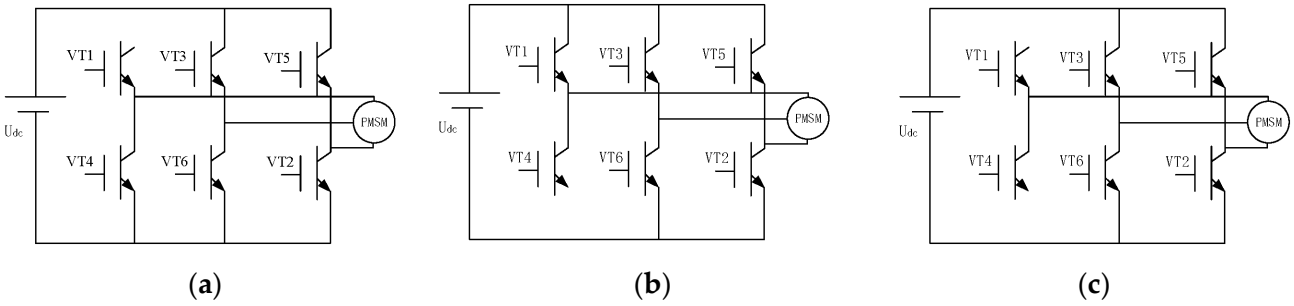

Figure 9. Schematic diagram of A-phase IGBT open circuit. (**a**) Open circuit of upper-bridge IGBT; (**b**) open circuit of lower-bridge IGBT. (**c**) Open circuit of both IGBT.

An IGBT open circuit of phase A is injected into the EMA simulator by disconnecting the IGBT(s) of this phase. The three-phase currents of the motor are generated (see Figures 10–12 for details). The open circuit of the upper-bridge IGBT causes current absence in the negative half-cycle, while that of the lower-bridge generates the current abnormality in the positive half-cycle. More precisely, the open circuit of both IGBTs indicates a winding disconnection in this phase.

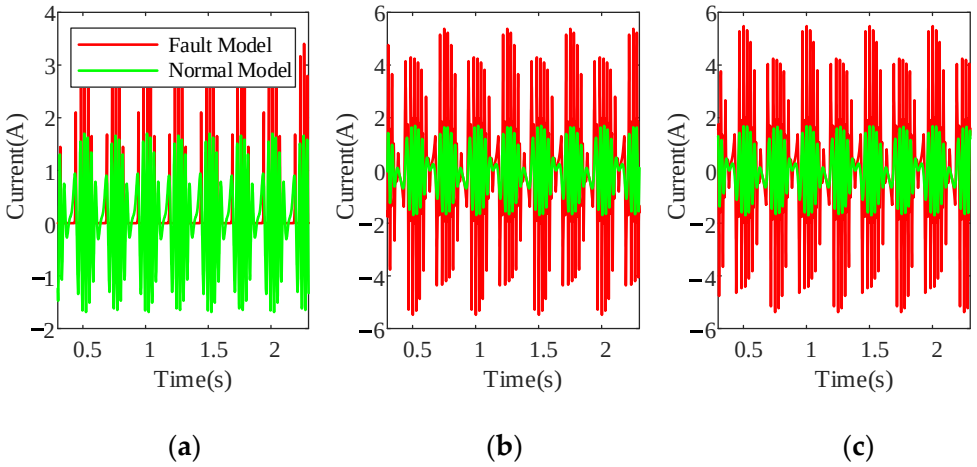

Figure 10. Fault data of A-phase upper-bridge IGBT open circuit. (**a**) A-phase current; (**b**) B-phase current. (**c**) C-phase current.

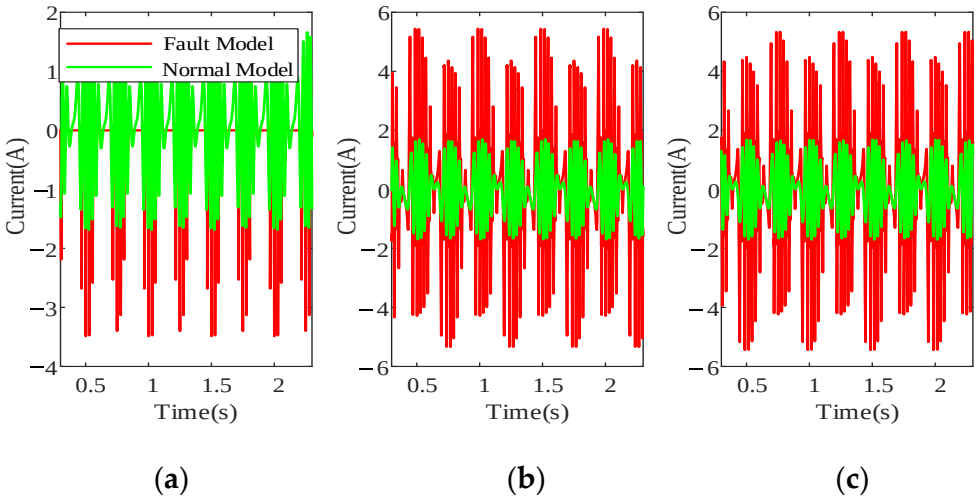

Figure 11. Fault data of A-phase lower-bridge IGBT open circuit. (**a**) A-phase current; (**b**) B-phase current. (**c**) C-phase current.

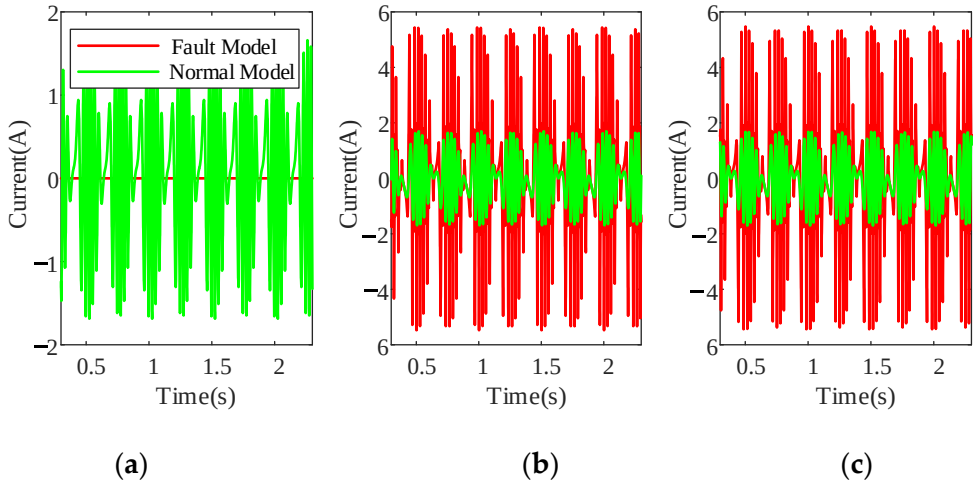

Figure 12. Fault data of A-phase both IGBT open circuits. (**a**) A-phase current; (**b**) B-phase current. (**c**) C-phase current.

Moreover, the sensor malfunction is also injected to validate the efficiency of the fault diagnosis method. On the contrary, the sensor malfunction is the most controllable to conduct on actual failure tests, due to the fact that it does not destroy the crucial component within the EMA structure. The sensor failures can lead to abnormal feedback of the closed-loop control and an unreliable system deviation. As illustrated in Figure 2, the EMA system involves a displacement sensor to detect the output rod displacement, a speed sensor to detect the motor speed, and a current sensor to detect the stator current. Theoretically, a sensor fault in the outer loop will result in a more uncontrollable system state. Therefore, the sensors' failures containing an open circuit of displacement sensor and a velocity sensor, are also injected into the EMA simulator to generate fault data. The three-phase current of the normal and failure conditions is generated (Figures 13 and 14). In addition, the reproduction of these sensor faults is implemented on the actual working EMA, which aims at demonstrating the validity of the fault diagnosis approach in practical use.

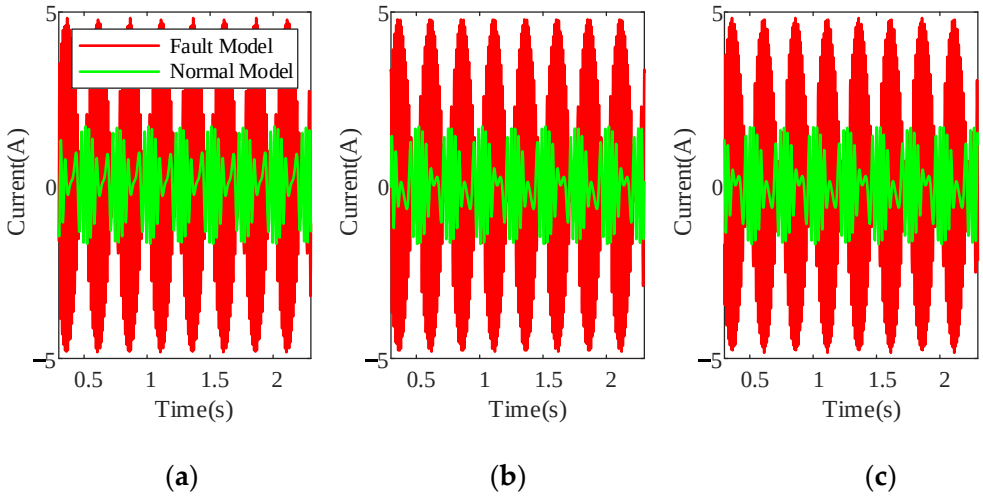

Figure 13. Fault data of displacement sensor open circuit. (**a**) A-phase current; (**b**) B-phase current. (**c**) C-phase current.

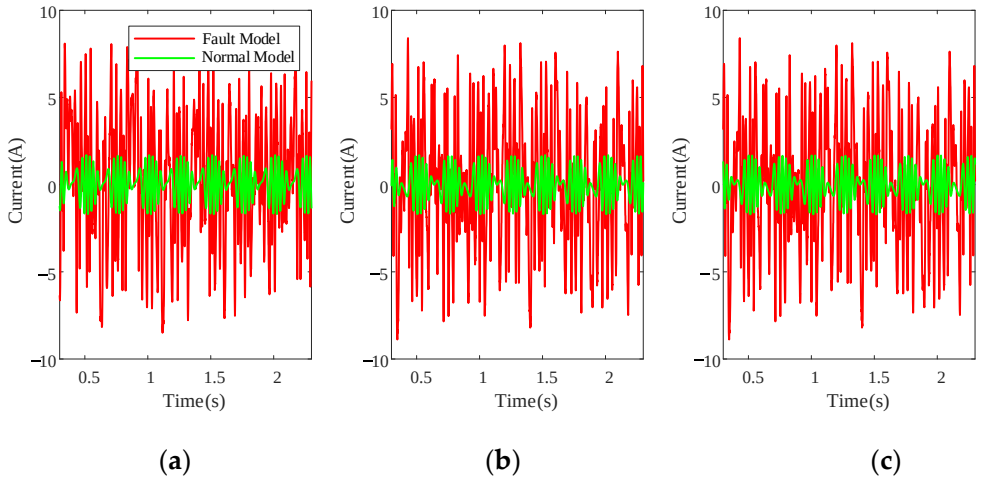

Figure 14. Fault data of velocity sensor open circuit. (**a**) A-phase current; (**b**) B-phase current. (**c**) C-phase current.

4.2. Fault Diagnosis Method Based on Gated Recurrent Unit (GRU) and Co-Attention Network

In this section, a network is proposed to identify the working state of the EMA under different conditions. The model is designed using the GRU and the co-attention mechanism, as shown in Figure 15.

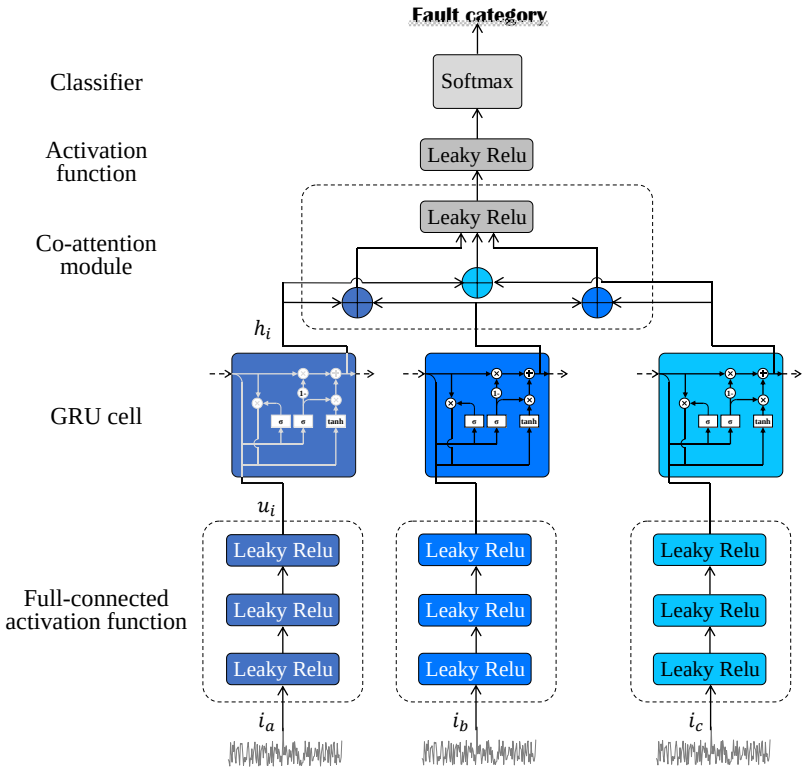

Figure 15. Fault diagnosis model architecture.

GRU is a variation of recurrent neural networks (RNNs) proposed by Cho et al. [35], which is generally used to learn sequential features from an input data stream using historical ones. A GRU is established on two gates and activation functions to integrate the previous memory into the current input, and thus update the output. The GRU is able to weaken the gradient vanish and get easily converged with a simple structure. On the other hand, the co-attention network deals with the interaction of different parts, and extracts the discriminative features from the input. In a deep-learning model, the integration of a co-attention mechanism aims at reducing the unrelated information and obtaining the essential information within the sequence. With respect to different types of sensing signals of the EMA simulator, the proposed model is based on the co-attention network, which aims at highlighting the significances of the time-varying and co-dependent data. The attentive information of each part is taken into account towards the final fault identification.

A given sequence of signals $X = [x_1, x_2, \cdots x_i, \cdots x_n] \in R^n$ is exactly detected from the coaxial-rotor unit. x_i is considered as the *ith* input vector of the proposed model. The input signals are fed into the three consecutive fully-connected layers to obtain sparse vectors while preserving features. For each layer, the leaky-Rectified Linear Unit (leaky-ReLU) function is used to activate the feature of x_i. The leaky-ReLU is expressed as:

$$leakyReLU = \begin{cases} x & x \geq 0 \\ leak * \min(0, x) & x < 0 \end{cases} \tag{7}$$

where *leak* represents the function slope for a negative input, which is generally a constant between 0 and 1, set to 0.2 in the proposed model.

Therefore:

$$x_i' = wx_i + b \tag{8}$$

and:

$$y_i = leakyReLU(x_i') \tag{9}$$

where w is the weight matrix and b is the bias vector. Both parameters are determined by model training.

Similarly, y_i is considered as the input of the following two-layer activation and thus an h_i is obtained:

$$z_i = leakyReLU(wy_i + b) \tag{10}$$

$$u_i = laekyReLU(wz_i + b) \tag{11}$$

Hence, features of the inputs can be thoroughly gleaned.

As previously mentioned, the sensing signals are encoded by GRU to capture the internal characteristics of the working state in time-sequence. For the vector u_i sent to a GRU cell, the previous information from the last hidden unit is integrated. Consequently, the output h_i is generated:

$$h_i = GRU(u_i) \tag{12}$$

h_i is kept as the hidden representation for the next-step processing within its GRU cell. At this stage, considering the input sequence of $X = [x_1, x_2, \cdots x_i, \cdots x_n]$, the corresponding set $H = [h_1, h_2, \cdots h_i, \cdots h_n]$ is obtained.

With an increasing amount of detected sensing data, a more accurate description of the working system can be accessed. Nevertheless, the more input signals are collected, the more complicated the processing procedures will be. In this paper, since all the data are sensed to characterize the working state, the three-phase current signals are fused to facilitate the processing rather than neglecting any important information. The co-attention mechanism is then performed to eliminate the irrelevant properties and obtain the essential features. Considering the interaction among different working parts in the system, the sensing signals on each part apparently affect the other sensor outcomes, and vice versa. For the vectors h_i and h_j, the attentive weight matrix can be calculated based on the interactive learning of the co-attention network:

$$W = leakyReLU\left(h_i^T M h_j\right) \tag{13}$$

where $M \in R^{n \times n}$ represents the parameter matrix and h_i^T denotes the transpose of h_i.

Furthermore, for the current sequence $H = [h_1, h_2, \cdots h_i, \cdots h_n]$, the attention mechanism is given by:

$$R = W\left(H^T\right) + B \tag{14}$$

where B is the bias matrix that is finetuned during the training process.

At this stage, the outcome vector R with the basic feature of the system, is sent to a softmax classifier to identify the working conditions:

$$o = softmax(R) \tag{15}$$

and:

$$\alpha_i = softmax(\beta_i) = \frac{exp(\beta_i)}{\sum_{k=1}^{C} exp(\beta_k)} \tag{16}$$

where C represents the number of different working conditions.

Thus, the fault classification result is given by:

$$O = (o)^T \tag{17}$$

4.3. Model Training

The training process of the proposed model is performed using the cross entropy and L_2 regularization as the loss function:

$$J = -\sum_{i=1}^{C} g_i log(y_i) + \lambda_r \left(\sum_{\theta \in \Theta} \theta^2\right) \tag{18}$$

where g_i is the real distribution of sentiment, y_i is the predicted one, and λ_r is the weight of L_2 regularization.

The gradients as well as the other parameters are updated by back propagation with the learning rate λ_l:

$$\Theta = \Theta - \lambda_l \frac{\partial J(\Theta)}{\partial \Theta} \tag{19}$$

5. Experiments

5.1. Experimental Setting

Experiments are conducted to verify the efficiency of the proposed fault diagnosis method. As previously mentioned, the model inputs are three-phase current signals that describe the EMA working states. Two general categories of failures (i.e., open circuit of motor and sensor malfunction) are simulated. The former contains 9 distinguishing faults while the latter contains 2 faults. Since 40 different working conditions exist, 440 sets of fault data and 40 sets of normal data are generated. Data of every single working state are simulated for 3 s, with a frequency of 1 kHz. For each data set, 1024 points of data are randomly picked in time sequence. In addition, for each data point, the following 512 points are considered as a data sample for further processing. Consequently, 491,520 (1024×480) sets of data are generated. All the samples are subdivided into the sets of training, validating, and testing with a ratio of 8:1:1.

The proposed model is finetuned with an ADAM optimizer with $\beta_1 = 0.9$, $\beta_2 = 0.999$ and $\varepsilon = 1 \times 10^{-8}$. The initialization parameters are used for 1000 iterations to optimize the related parameters. All the parameter matrices are randomly generated in the distribution of $U\ (-0.1,\ 0.1)$, while the bias is initialized to 0. The hidden states dimension of the GRU cell is set to 300, with a learning rate of 0.001. Both the batchsize and the training epoch are set to 10. Moreover, the L_2 regularization weight is set to 0.0001, and the dropout rate is set to 0.5 to prevent overfitting.

5.2. Results

In this experiment, the accuracy is considered as the evaluation metric used to characterize the working performance. Table 2 presents the testing accuracy of each fault diagnosis task, for each working condition.

Table 2. Fault diagnosis accuracy.

Fault Category		Accuracy
Motor stator open circuit	A-phase open circuit	98.0%
	B-phase open circuit	97.9%
	C-phase open circuit	97.5%
Motor driver open circuit	A-phase upper-bridge IGBT open circuit	98.6%
	A-phase lower-bridge IGBT open circuit	98.2%
	B-phase upper-bridge IGBT open circuit	98.2%
	B-phase lower-bridge IGBT open circuit	98.1%
	C-phase upper-bridge IGBT open circuit	98.0%
	C-phase lower-bridge IGBT open circuit	98.2%
Sensor malfunction	Displacement sensor open circuit	95.9%
	Velocity sensor open circuit	95.9%
Normal state		97.8%

Among all the evaluation settings, the motor driver open circuit diagnosis has the best and most consistent performance compared to that of the other methods. The accuracy of the motor driver open circuit classification ranges between 98.0% and 98.6%. The best-performing outcome in this group is the diagnosis of the A-phase upper-bridge IGBT open circuit. The results obtained on motor stator open circuit range from 97.5% to 98.0%, and

therefore they are slightly lower than those obtained on motor driver open circuit. In addition, the diagnosis accuracy of sensor malfunction and normal state are 95.9% and 97.8%, respectively. Consequently, the experimental results in Table 2 demonstrate the universality of the proposed model, due to the accuracy consistency in different working conditions.

5.3. Experimental Verification

In this experiment, the sensor failure is used for representation to perform the actual experimental setup, which aims at identifying the outperformance of the proposed model. The test rig is illustrated in Figure 16. To confirm the consistency of the proposed simulator and the actual EMA, time-domain and frequency-domain analysis are conducted. Figure 17 presents the tracking responses to a 1 Hz sinusoidal signal of both simulated and actual EMAs, with a tracking error within 0.1 mm. According to the bode diagram of Figure 18, the similarity between the two EMAs reaches 95%, which demonstrates the efficiency of the EMA simulator in fault data generation.

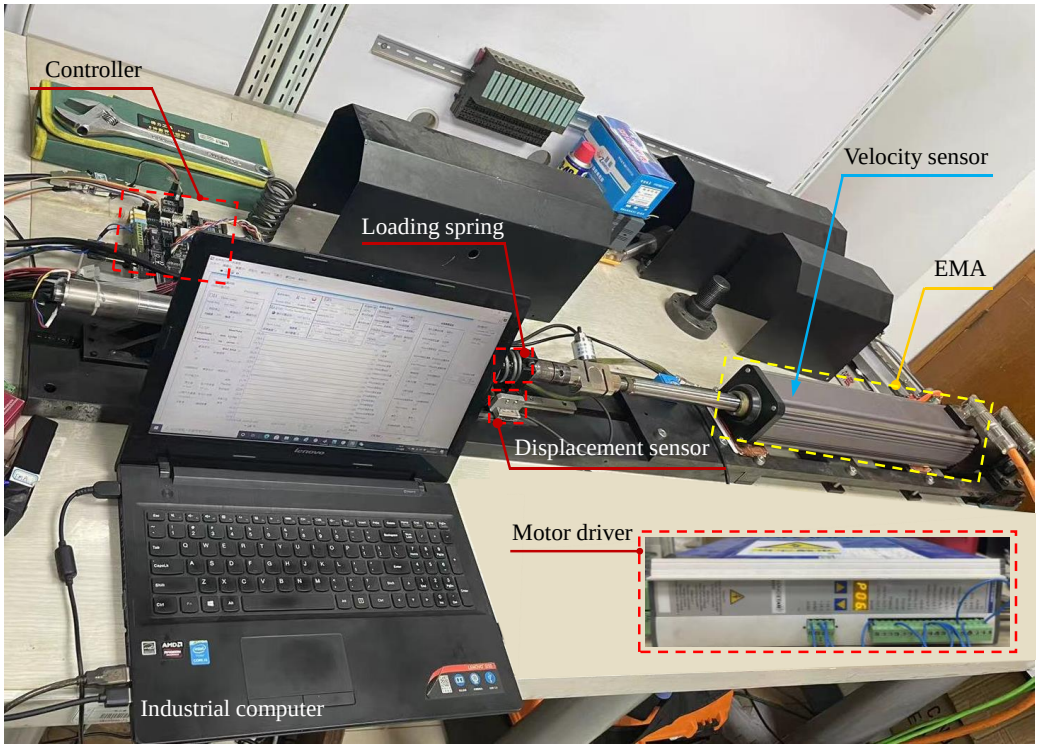

Figure 16. The test rig.

The velocity sensor is embedded into the EMA structure.

According to the simulation-based outcomes, no-load working state has a sinusoidal signal as the control command with a 2 mm amplitude and 0.6 Hz to 1.8 Hz frequencies and an interval of 0.3 Hz. Under this condition, a spring is further taken to apply a 500 N external load to the EMA. The failures can be regenerated by disconnecting the sensing cables of the displacement sensor. The normal state and the sensor malfunction are performed with a total number of 20 working conditions. For each working condition, the data sequence contains 1024 sets of three-phase currents of the motor, that are collected as test samples and sent to the fault diagnosis method.

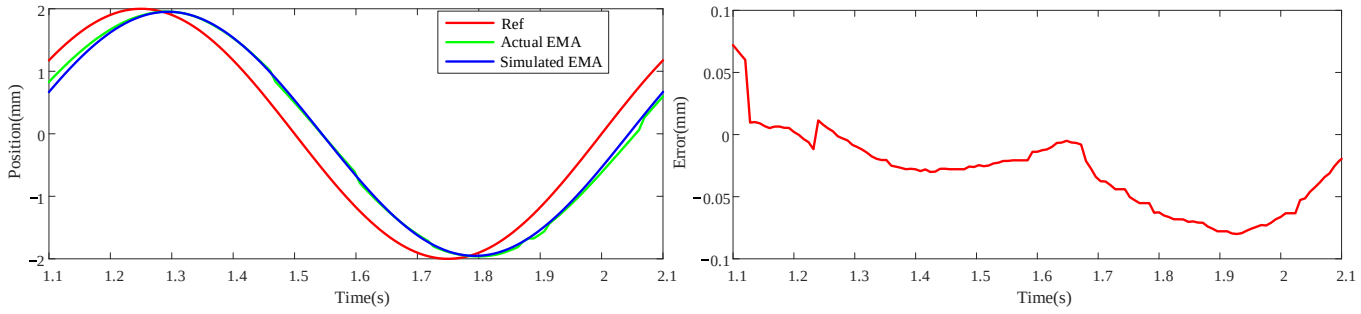

(**a**) (**b**)

Figure 17. Time domain analysis of simulated and actual EMA. (**a**) Response to a 1 Hz sinusoidal signal; (**b**) response error.

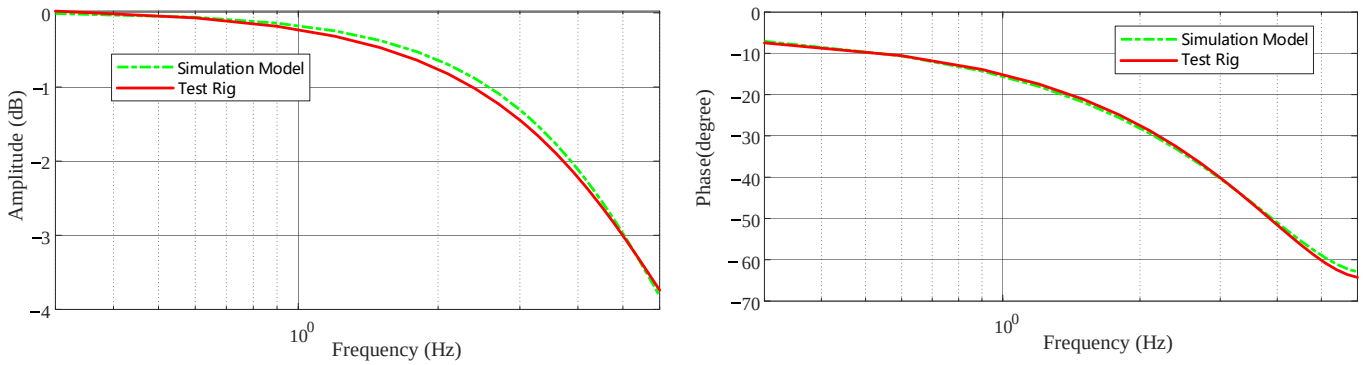

(**a**) (**b**)

Figure 18. Frequency domain analysis of simulated and actual EMA. (**a**) Amplitude margin; (**b**) phase margin.

The testing results are presented in Figure 19. The average classification accuracy of the proposed model is 89.4%, where 90.7% are for normal state and 88.1% for sensor malfunction. When a failure occurs in the actual system, the current signals variation is of the same property with that of the simulation data. In addition, only if multiple data sequences representing a fault are simultaneously detected, the working state can be determined as a fault. Consequently, a satisfying fault diagnosis accuracy is still accessible. The proposed model fails to retain the performance of the simulating experimental outcomes. This is due to the fact that the three-phase current of the motor in the actual system contains noise, which can introduce measurement errors into the signals. Notably, the variation of input signals merely results in a marginal drop of the classification accuracy, which indicates the stability of the proposed model. Since the proposed model is able to classify faults on actual working systems by simulated data training, it is reasonable to expect better performance in practical use.

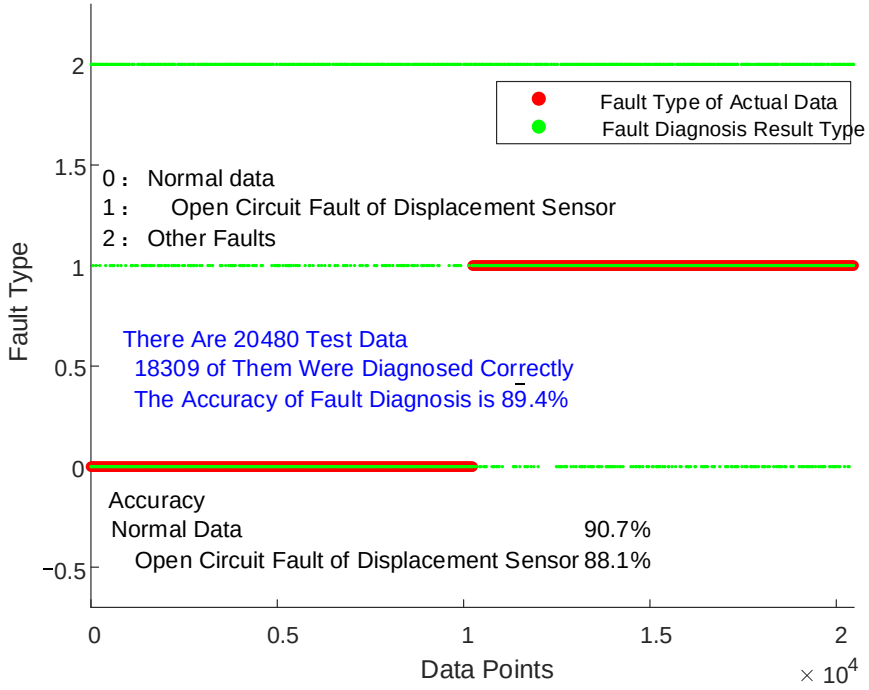

Figure 19. Experimental results obtained on the actual EMA.

5.4. Discussion

The data detected from an actual EMA system is also sent to more fault diagnosis methods for working performance comparison. To be specific, the recurrent neural network (RNN) and the long short-term memory (LSTM) are taken to substitute the GRU in the proposed model. The fault classification results are given in Table 3.

Table 3. Fault classification accuracy of different algorithm.

Model	RNN	LSTM	GRU
Average	87.53%	90.76%	89.4%
Normal state	91.58%	92.47%	90.7%
Sensor malfunction	84.39%	89.20%	88.1%

Apparently, our model outperforms RNN on the average classification accuracy. By contrast, the application of LSTM has a slightly better performance than our model. Both LSTM and GRU are the variants of basic RNN. Thus, it is acceptable that the outcomes of LSTM- and GRU-based models are comparable. With more training data detected, the model can be developed in a more effective way, as it is the case.

6. Conclusions

This paper proposed a methodology on the task of EMA fault diagnosis. A virtual model of EMA which is in line with the actual EMA, is first developed to simulate its working states. The fault data corresponding to the actual failures in EMA are then injected into the EMA simulator to generate fault signals for processing. Moreover, a deep-learning-based approach is developed for the diagnosis of faults based on working states classification. In this fault diagnosis model, the GRU cells are used to capture the characteristics of different states while a co-attention network is used to remove the unrelated features and integrate the discriminative information. The performance of the proposed model is validated on three categories of working states. The experimental results demonstrate that the proposed model achieves a higher accuracy (by 95.0%) for all the evaluation settings. Furthermore, the verification of the fault diagnosis model on actual EMA is also performed, which further confirms the efficiency in practical use.

Since the collection of all the failures of EMA is too complicated, it is impossible to detect faults of all the categories. The diagnosis of an increasing number of faults requires further studies. Although the proposed model can classify the working state of EMA due to the current simulation model and laboratory condition, the possibility of further accurate identification of more faults is still an open question.

Author Contributions: Conceptualization, Z.P. (Zhaoqin Peng) and J.C.; methodology, Z.S.; validation, Z.S., Z.P. (Zilong Ping); formal analysis, Z.S. and K.D.; investigation, Z.S. and K.D.; data curation, Z.S.; writing—original draft preparation, Z.P. (Zhaoqin Peng); writing—review and editing, E.Z.; visualization, J.L.; supervision, Z.P. (Zilong Ping); project administration, J.C.; funding acquisition, Y.F. All authors have read and agreed to the published version of the manuscript.

Funding: This research received no external funding.

Institutional Review Board Statement: Not applicable.

Informed Consent Statement: Not applicable.

Data Availability Statement: Not applicable.

Conflicts of Interest: The authors declare no conflict of interest.

References

1. Gunter, S.; Buticchi, G.; Carne, G.D.; Gu, C.; Liserre, M.; Zhang, H.; Gerada, C. Load Control for the DC Electrical Power Distribution System of the More Electric Aircraft. *IEEE Trans. Power Electron.* **2018**, *34*, 3937–3947. [CrossRef]
2. Wang, Y.; Nuzzo, S.; Zhang, H.; Zhao, W.; Gerada, C.; Galea, M. Challenges and Opportunities for Wound Field Synchronous Generators in Future More Electric Aircraft. *IEEE Trans. Transp. Electrif.* **2020**, *6*, 1466–1477. [CrossRef]
3. Villani, M.A.; Tursini, M.; Fabri, G.; Castellini, L. Electromechanical Actuator for Helicopter Rotor Damper Application. *IEEE Trans. Ind. Appl.* **2014**, *50*, 1007–1014. [CrossRef]
4. Nelson, T. *787 Systems and Performance*; The Boeing Company: Chicago, IL, USA, 2005; pp. 1–36. Available online: https://myhres.com/Boeing-787-Systems-and-Performance.pdf (accessed on 20 February 2021).
5. Derrien, J.C.; Sécurité, S.D. Electromechanical actuator (EMA) advanced technologies for flight controls. In Proceedings of the 28th International Congress of the Aeronautical Sciences, Brisbane, Australia, 23–28 September 2012; pp. 1–13.
6. Giangrande, P.; Galassini, A.; Papadopoulos, S.; Al-Timimy, A.; Calzo, G.L.; Degano, M.; Galea, M.; Gerada, C. Considerations on the Development of an Electric Drive for a Secondary Flight Control Electromechanical Actuator. *IEEE Trans. Ind. Appl.* **2019**, *55*, 3544–3554. [CrossRef]
7. Bennett, J.W.; Mecrow, B.C.; Atkinson, D.J.; Maxwell, C.; Benarous, M. Fault-tolerant electric drive for an aircraft nose wheel steering actuator. *IET Electr. Syst. Transp.* **2010**, *1*, 117–125. [CrossRef]
8. Maleki, S.; Bingham, C.; Yu, Z. Development and Realization of Changepoint Analysis for the Detection of Emerging Faults on Industrial Systems. *IEEE Trans. Ind. Inform.* **2016**, *12*, 1180–1187. [CrossRef]
9. Cao, Y.; Lyu, Y.; Wang, X. Fault Diagnosis Reasoning Algorithm for Electromechanical Actuator Based on an Improved Hybrid TFPG Model. *Electronics* **2020**, *9*, 2153. [CrossRef]
10. Gao, Z.; Cecati, C.; Ding, S.X. A Survey of Fault Diagnosis and Fault-Tolerant Techniques—Part II: Fault Diagnosis with Knowledge-Based and Hybrid/Active Approaches. *IEEE Trans. Ind. Electron.* **2015**, *62*, 3768–3774. [CrossRef]
11. Mercorelli, P. A Fault Detection and Data Reconciliation Algorithm in Technical Processes with the Help of Haar Wavelets Packets. *Algorithms* **2017**, *10*, 13. [CrossRef]
12. Wang, D. K-nearest neighbors based methods for identification of different gear crack levels under different motor speeds and loads: Revisited. *Mech. Syst. Signal Process.* **2016**, *70*, 201–208. [CrossRef]
13. Baraldi, P.; Podofillini, L.; Mkrtchyan, L.; Zio, E.; Dang, V. Comparing the treatment of uncertainty in bayesian networks and fuzzy expert systems used for a human reliability analysis application. *Reliab. Eng. Syst. Saf.* **2015**, *138*, 176–193. [CrossRef]
14. Vapnik, V.N. *The Nature of Statistical Learning Theory*; Springer Science & Business Media: Berlin, Germany, 2013.
15. Wang, X.; Liu, X.; Song, P.; Li, Y.; Qie, Y. A Novel Deep Learning Model for Mechanical Rotating Parts Fault Diagnosis Based on Optimal Transport and Generative Adversarial Networks. *Actuators* **2021**, *10*, 146. [CrossRef]
16. Martini, D.D.; Facchinetti, T. Fault Detection of Electromechanical Actuators via Automatic Generation of a Fuzzy Index. *IEEE/ASME Trans. Mechatron.* **2020**, *25*, 2197–2207. [CrossRef]
17. Zhang, X.; Tang, L.; Chen, J. Fault Diagnosis for Electro-Mechanical Actuators Based on STL-HSTA-GRU and SM. *IEEE Trans. Instrum. Meas.* **2021**, *70*, 3527716. [CrossRef]
18. Siahpour, S.; Li, X.; Lee, J. Deep learning-based cross-sensor domain adaptation for fault diagnosis of electro-mechanical actuators. *Int. J. Dyn. Control.* **2020**, *8*, 1054–1062. [CrossRef]
19. Yang, J.; Guo, Y.; Zhao, W. An intelligent fault diagnosis method for an electromechanical actuator based on sparse feature and long short-term network. *Meas. Sci. Technol.* **2021**, *32*, 095102. [CrossRef]

20. Yu, M.; Xiao, C.; Jiang, W.; Yang, S.; Wang, H. Fault Diagnosis for Electromechanical System via Extended Analytical Redundancy Relations. *IEEE Trans. Ind. Inform.* **2018**, *14*, 5233–5244. [CrossRef]
21. Balaban, E.; Bansal, P.; Stoelting, P.; Saxena, A.; Goebel, K.F.; Curran, S. A diagnostic approach for electro-mechanical actuators in aerospace systems. In Proceedings of the 2009 IEEE Aerospace Conference, Big Sky, MT, USA, 7–14 March 2009; pp. 1–13.
22. Wang, C.; Tao, L.; Ding, Y.; Lu, C.; Ma, J. An adversarial model for electromechanical actuator fault diagnosis under nonideal data conditions. In *Neural Computing and Applications*; Springer: Berlin, Germany, 2022.
23. Mariani, A.; Pellegrini, E.; Momi, E.D. Skill-oriented and Performance-driven Adaptive Curricula for Training in Robot-Assisted Surgery using Simulators: A Feasibility Study. *IEEE Trans. Biomed. Eng.* **2020**, *68*, 685–694. [CrossRef]
24. Fernandes, P.; Pinheiro, A.; Cruz, G.; Maia, A.; Morgado, L.; Martins, P.; Paredes, H.; Fonseca, B.; Lopes, J.B.; Cravino, J. Multi-user virtual world simulator of F-16 aircraft engine mechanical maintenance. In Proceedings of the 2013 2nd Experiment@ International Conference, Coimbra, Portugal, 18–20 September 2013; pp. 166–167.
25. Ram, M.S.; Sumanth, K.; Jawaharlal, B. Design and Simulation study of Electro-Mechanical Actuator for Missile Maneuvering. *Int. J. Sci. Res. Publ.* **2020**, *10*, 225–232.
26. Qiao, G.; Liu, G.; Shi, Z.; Wang, Y.; Ma, S.; Lim, T.C. A review of electromechanical actuators for More/All Electric aircraft systems. *J. Mech. Eng. Sci.* **2018**, *232*, 4128–4151. [CrossRef]
27. Li, Y. Posture Control of Electromechanical-Actuator-Based Thrust Vector System for Aircraft Engine. *IEEE Trans. Ind. Electron.* **2012**, *59*, 3561–3571. [CrossRef]
28. Giangrande, P.; Madonna, V.; Sala, G.; Kladas, A.; Gerada, C.; Galea, M. Design and Testing of PMSM for Aerospace EMA Applications. In Proceedings of the IECON 2018 44th Annual Conference of the IEEE Industrial Electronics Society, Washington, DC, USA, 21–23 October 2018; pp. 2038–2043.
29. Vanathy, B.; Dikshit, V.G.; Hotkar, V.G.; Reddy, S.K.; Jacob, A. Design and Development of Digital Controller for Airborne Electro Mechanical Actuators. In Proceedings of the 2018 Fourth International Conference on Computing Communication Control and Automation, Pune, India, 16–18 August 2018; pp. 1–6.
30. Jensen, S.C.; Jenney, G.D.; Dawson, D. Flight test experience with an electromechanical actuator on the F-18 Systems Research Aircraft. In Proceedings of the 19th Digital Avionics Systems Conference (DASC), Philadelphia, PA, USA, 7–13 October 2000; Volume 1, p. 2E3/1-2E310.
31. *In-Service Reliability Data of Continuously Active Ballscrew and Geared Flight Control Actuation Systems*; AIR5713; SAE Aerospace: Warrendale, Pennsylvania, 2006.
32. Zhang, Y.; Peng, Y.; Liu, L. Degradation Estimation of Electro-Mechanical Actuator with Multiple Failure Modes Using Integrated Health Indicators. *IEEE Sens. J.* **2020**, *20*, 7216–7225. [CrossRef]
33. Rauf, H.T.; Bangyal, W.; Lali, M.I. An adaptive hybrid differential evolution algorithm for continuous optimization and classification problems. *Neural Comput. Appl.* **2021**, *33*, 10841–10867. [CrossRef]
34. Price, K.V. Differential Evolution [M]. In *Handbook of Optimization*; Springer: Berlin/Heidelberg, Germany, 2013; pp. 187–214.
35. Cho, K.; van Merrienboer, B.; Gulcehre, C.; Bahdanau, D.; Bougares, F.; Schwenk, H.; Bengio, Y. Learning Phrase Representations using RNN Encoder-Decoder for Statistical Machine Translation. *arXiv* **2014**, arXiv:1406.1078.